Internal quantum efficiency in 6.1 Å superlattices of 77% for mid-wave infrared emitters

Cite as: Appl. Phys. Lett. 117, 061101 (2020); https://doi.org/10.1063/5.0013854 Submitted: 14 May 2020 . Accepted: 25 July 2020 . Published Online: 10 August 2020

🗓 A. J. Muhowski, A. M. Muellerleile, J. T. Olesberg, and 🗓 J. P. Prineas







ARTICLES YOU MAY BE INTERESTED IN

Minority carrier lifetime and photoluminescence of mid-wave infrared InAsSbBi Applied Physics Letters 117, 061103 (2020); https://doi.org/10.1063/5.0007275

Quantum size effect in nanocorrals: From fundamental to potential applications Applied Physics Letters 117, 060501 (2020); https://doi.org/10.1063/5.0015542

Toward high efficiency tin perovskite solar cells: A perspective Applied Physics Letters 117, 060502 (2020); https://doi.org/10.1063/5.0014804





Internal quantum efficiency in 6.1 Å superlattices of 77% for mid-wave infrared emitters

Cite as: Appl. Phys. Lett. 117, 061101 (2020); doi: 10.1063/5.0013854 Submitted: 14 May 2020 · Accepted: 25 July 2020 · Published Online: 10 August 2020







A. J. Muhowski, ^{1,2} (1) A. M. Muellerleile, ^{1,2} J. T. Olesberg, ^{1,2} and J. P. Prineas ^{1,2,3,a)} (1)

AFFILIATIONS

- Department of Physics and Astronomy, University of Iowa, Iowa City, Iowa 52242, USA
- ²Iowa CREATES, University of Iowa, Iowa City, Iowa 52242, USA
- ³Department of Electrical and Computer Engineering, University of Iowa, Iowa City, Iowa 52242, USA

ABSTRACT

Two new superlattices with high internal quantum efficiency at high injection, InAs/AlGaInSb and InAs/GaInSb/InAs/AlAsSb, are presented and compared with state-of-the-art InAs/GaSb and InAs/InAsSb superlattices. The internal quantum efficiency peaks at 44% and 77% for the InAs/AlGaInSb and InAs/GaInSb/InAs/AlAsSb samples, respectively, which suggests that they are excellent candidates for highefficiency mid-wave infrared LEDs. These values have been measured without invoking the ABC model to eliminate the assumption of Boltzmann statistics. The calculated superlattice band structures are used qualitatively to explain the internal quantum efficiency results.

Published under license by AIP Publishing. https://doi.org/10.1063/5.0013854

Mid-wave infrared LEDs based on 6.1 Å III/V semiconductors, in contrast to LEDs in more developed wavelength ranges and material families, have exceedingly low efficiency. Wallplug efficiency (the ratio of optical output power to electrical input power) for the highest performance LEDs approaches only 0.7% at 80 K. This is often attributed to the low light-extraction efficiency $(1/4n^2 \approx 2\%)$; however, a significant part of this inefficiency comes from the low internal quantum efficiency of the active region, which measures the portion of excited carriers that recombine radiatively and produce photons. Internal quantum efficiencies are severely limited by high Auger non-radiative recombination at high injection, which outcompetes the radiative process in many emitters. 1,3,4 Previously, we have shown that the internal quantum efficiency of InAs/GaSb superlattices in the mid-wave infrared peaks near 30% for 77 K operation. Thermal scene projection, the principal driver for high-efficiency mid-wave infrared LEDs, requires cryogenic operation to reduce the radiated blackbody power of the projector system below the noise-equivalent power of the detection system such that the thermal accuracy of each scene is limited by detector performance. Moreover, cryogenic operation is a precursor to optimized ambient-temperature operation for applications such as gas sensing and free-space optical communications.

Early detector efforts involving type-II superlattices employed InAs/Ga(In)Sb superlattices as absorber regions.7 Initial predictions suggested that the small effective mass in InAs/Ga(In)Sb superlattices would yield lower dark currents compared to MCT detector active regions;8 however, dark currents in InAs/Ga(In)Sb superlattice detectors were instead limited by short Shockley-Read-Hall times. Type-II superlattice detector efforts have shifted within the past decade to InAs/InAsSb active regions and their 100× longer Shockley-Read-Hall times compared to the InAs/Ga(In)Sb systems;^{9,10} early reports of InGaAs/InAsSb promise further improvements from higher absorption coefficients. 11,12

While detector efforts have pursued progressively better performance with new superlattices, superlattice emitter efforts have remained focused on InAs/GaSb superlattices. Other emitter designs based on quantum wells have been employed extensively in type-I laser diodes and type-II interband cascade lasers because strain-induced hole-state splitting reduces the density-of-states imbalance with commensurate reductions in the threshold carrier densities. 13-15 These designs have often been used as LEDs. 16-19 InAs/GaSb superlattices remain a state-ofthe-art emission region for high radiance LEDs.^{20,21}

Here, we present two superlattice designs [InAs/AlGaInSb and InAs/GaInSb/InAs/AlAsSb (W-SL)] with high internal quantum efficiency and compare with state-of-the-art InAs/InAsSb and InAs/GaSb superlattices. These measurements are performed in a manner that does not assume the validity of the ABC model or Boltzmann statistics. Each of the former three superlattices has greater internal quantum efficiency than InAs/GaSb, and the first two have not been employed in superlattice LEDs where their increased internal quantum efficiency may be beneficial.

a) Author to whom correspondence should be addressed: john-prineas@uiowa.edu

Superlattices have much larger parameter spaces than conventional alloys. For instance, $InAs/InAs_xSb_{1-x}$ superlattices have a threedimensional compositional space (i.e., two thicknesses and one alloy composition parameter), while the ternary alloy $InAs_xSb_{1-x}$ has a onedimensional compositional space. Each of these spaces are reduced by one dimension when the system is constrained to be lattice-matched to a particular substrate, leaving a two-dimensional space of InAs/ In AsSb superlattices that are lattice-matched to a GaSb substrate and a zero-dimensional space (i.e., a single point) for ternary InAsSb. This lends great tunability to superlattices in comparison to bulk alloys and creates the possibility of improving characteristics and performance; however, the large phase space leaves much to be explored. In the mid-wave infrared, InAs/GaSb and InAs/InAsSb structures with high quantum efficiency/low Auger have previously been identified, particularly in Refs. 5 and 22, respectively. InAs/AlGaInSb and the W-SL have not been systematically explored. The latter has been used for detector and laser applications, 23,24 and quantum well variants with a reduced active region volume have seen great success in interband cascade lasers. 13,14 Here, a series of samples were grown with different hole well thicknesses for both InAs/AlGaInSb and the W-SL to systematically vary the valence band structure, and the optimal superlattice for each design family was selected as in Ref. 5. Compositional parameters and calculated dipole matrix elements P for transverseelectric polarized emission are given in Table I.

Auger recombination must be minimized, and radiative recombination must be maximized in order to achieve high internal quantum efficiency for spontaneous emission, which is equivalent to reducing the number of electronic states near certain points in the band structure and increasing the dipole matrix element of the radiative transition. Auger recombination excites carriers deeper into their respective bands, and the majority of carriers reside at the band edges. Consequently, the most detrimental higher-energy band locations for Auger recombination occur at the Auger resonance energies one bandgap above the conduction band edge and one bandgap below the valence band edge. To suppress Auger processes, bands should be moved away from the Auger resonance energies such that the Auger transitions are forbidden. The dipole matrix element appears in the Fermi's Golden Rule expression for the radiative rate, with larger dipole matrix elements yielding higher radiative rates.

TABLE I. Compositional parameters and calculated momentum matrix elements for each superlattice.

Sample	Layers (Å)	Thickness (Å)	$\frac{2P^2}{m_0}$ (eV)
A	InAs	24	2.09
	GaSb	48	
В	InAs	30.1	5.05
	$In As_{0.66}Sb_{0.34}$	9.8	
С	InAs	25	2.22
	$\text{Al}_{0.1}\text{Ga}_{0.84}\text{In}_{0.06}\text{Sb}$	39	
D	InAs	17.1	2.69
	$Ga_{0.7}In_{0.3}Sb$	27	
	InAs	17.1	
	$AlAs_{0.27}Sb_{0.73}$	18	

This framework can be applied to the superlattice band structures and dipole matrix elements as calculated by 14-band superlattice $K \cdot p$, shown in Fig. 1 and listed in Table I. Sample A represents a baseline for the dipole matrix element and proximity of states to the Auger resonances, as this is a high performance active region that has been used extensively in mid-wave infrared LEDs. Sample B has more than twice the dipole matrix element compared to sample A due to the strong overlap of the weakly confined electron state and highest heavy-hole state; however, there are multiple states in close proximity to the valence band Auger resonance, suggesting high radiative and Auger recombination rates. There is very little relative offset between the InAs and InAsSb layers, providing no hole confinement in the InAsSb layer at the valence band Auger resonance energy to suppress states, analogous to the continuum states that form above a finite square-well potential. Sample C is very similar to sample A as the hole-well layer in sample C is predominantly GaSb. However, the thinner quaternary hole-well layer results in a slightly increased wave function overlap corresponding to a 6% increase in the dipole matrix element. The added quantum confinement pushes the second highest light-hole state out of the hole well and third highest heavy-hole state below the Auger resonance energy. Sample D has a 29% increase in the dipole matrix element compared to sample A due to the penetration of the electron state into GaInSb and has few states near the valence band Auger resonance, suggesting improvements to the internal quantum efficiency from both an enhanced radiative rate and a suppressed Auger rate. Both effects derive from the thin GaInSb layer. Additionally, the AlAsSb barrier increases penetration of the electron state into the GaInSb layer and compensates the high strain in the GaInSb, which clears light-hole states out of the hole well.

Each superlattice was grown via molecular beam epitaxy using a Veeco Gen-20 reactor, with valved As and Sb sources operating in a monomeric regime. Ga, In, and Al were supplied by SUMO cells. Growth rates for each alloy were 0.6ML/s except AlGaInSb which was

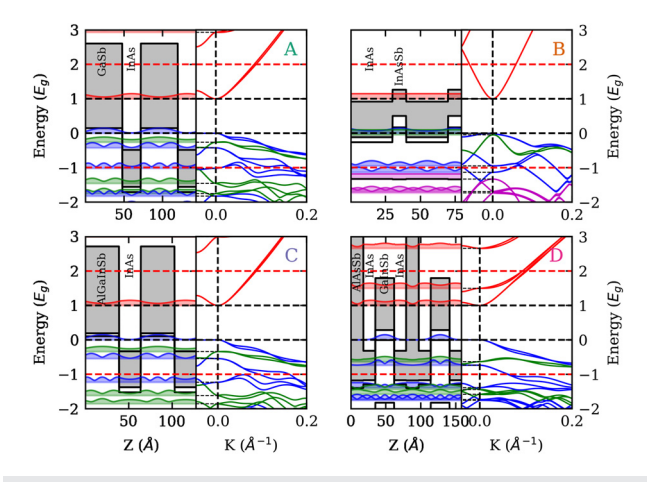


FIG. 1. Bulk band edges (shaded gray regions) overlaid with zone-center envelope functions (left) and superlattice band structures (right) for samples A, B, C, and D. Red, blue, green, and magenta correspond to conduction band, heavy-hole, lighthole, and split-off-hole states, respectively, for the envelope functions and superlattice bands. Negative K represent wavevectors in the growth direction; positive represents in-plane wavevectors. The horizontal black and red dashed lines correspond to the band edges and Auger resonance energies, respectively.

grown at 1ML/s. Group V fluxes were held 30% higher than required for III-limited growth. Samples were grown on lightly doped Te:GaSb substrates ($n \sim 1.5 \times 10^{17} \text{ cm}^{-3}$) to minimize free-carrier absorption in the mid-wave infrared.²⁵ One quarter of a 50 mm GaSb substrate was outgassed at 250 °C prior to growth and thermally desorbed under Sb flux at 530 °C. A buffer layer comprising 150 nm GaSb, 30 nm lattice-matched AlAsSb, and 500 nm GaSb was grown before the active layers; each superlattice was surrounded by 30 nm AlAsSb clads and capped in 10 nm GaSb to prevent oxidation. Samples A, B, and C contained nominally 1 μ m thick superlattices, while sample D was nominally 500 nm thick. Sample D features a tightly bound highest heavy-hole state and a larger effective mass, which may adversely affect carrier transport and cause non-uniform excitation. An independent series of samples comprising identical superlattices to sample D with varying overall thicknesses was grown. It was empirically determined from photoluminescence measurements on those samples that 500 nm was a sufficiently thin W-SL active region for uniform carrier excitation given the pumping conditions described below.

Samples were cleaved into 5 mm × 10 mm pieces, mounted in a cryostat, and cooled to 77 K for testing. Photoluminescence, excited by 20 W/cm² from an 870 nm laser diode modulated at 25 kHz, was collected and directed through a commercial Fourier-transform interferometer (FTIR) and onto a cooled mercury-cadmium-telluride detector. The detected signal was then demodulated via a lock-in amplifier and passed to the FTIR control electronics to process the spectra. Photoluminescence spectra were collected in continuous scan mode. Internal quantum efficiency measurements were made in the same manner as Ref. 5. The radiance of the photoluminescence was measured via a calibrated, cooled InSb detector in a normally incident staring configuration and through an iris to block off-axis light reflected by the cryostat. The effective spectral responsivity of the InSb detector was taken to be the product of the vacuum detector responsivity, atmospheric transmittance including the 4.2 μ m CO₂ band, the transmittance of the ZnSe cryostat window, and the transmittance of a 2400 nm long-pass filter. The effective responsivity was then taken as an average value of the effective spectral responsivity weighted by the photoluminescence spectra for each sample. The 930 nm pump laser diode was angled with respect to the collection axis to prevent reflected pump photons from exciting the detector, while scattered pump photons were blocked by the 2400 nm long-pass filter mounted directly in front of the detector. The pump irradiance was varied by changing the drive current for the laser, varying the spot size, and introducing neutral-density filters.

The internal quantum efficiency has been measured by combining the emitted radiance, absorbed pump irradiance, and a calculated extraction efficiency. The radiance of the photoluminescence can be converted to a volumetric photon output rate that characterizes the amount of light emitted by the sample independent of the emission wavelength and sample thickness. Similarly, the input power of the pump beam can be converted to a volumetric carrier generation rate that is independent of the sample thickness and carrier lifetime. The absorption coefficient at the pump wavelength was taken as a weighted average of the constituent binary semiconductors. High above the band edge, the absorption coefficient is sufficiently large such that $\exp{(-\alpha D_{SL})}$ shows negligible changes for fairly wide variations in the absorption coefficient. Carriers then homogenize throughout the active regions, which has been shown to occur in similar superlattice

materials on time scales much shorter than the minority carrier lifetime even with high excitation and extremely above-bandgap pumping. An extraction efficiency can be calculated within a two-slab model from the thicknesses, indices, and absorption coefficients at the emission wavelength of the substrate and epilayer. For the substrate, these values are 500 μm , 3.8, and 3 cm $^{-1}$. The index for the epilayer has been taken to be the weighted average of the constituent binary semiconductors, and the absorption coefficient has been taken to be 0 cm $^{-1}$ as the active region is assumed to be pumped approximately transparency at the band edge. Additional details regarding the analysis are presented in Ref. 5.

The data in Fig. 2 show strong mid-wave infrared emission with approximately a factor of 2.5 improvement in peak internal quantum efficiency from sample A to sample D at 77 K and a factor of 4 at 293 K. The internal quantum efficiencies of each superlattice as a function of volumetric carrier generation rate G are reported in Figs. 2(b) and 2(e). Sample A exhibited the lowest peak internal quantum efficiency (29% at 77 K and 2.1% at 293 K) and the highest carrier generation rate for peak internal quantum efficiency. The internal quantum efficiency of samples C and D peaked at similar carrier generation rates with peak internal quantum efficiencies of 44% and 77% at cryogenic temperatures, while the room-temperature values were 3.1% and 8.5%, respectively. The peak internal quantum efficiency of sample B occurs below the minimum level of excitation tested and is, therefore, unknown. However, the internal quantum efficiency of sample B is lower than that of the other samples in the tested range, with the exception of samples A and C at low injection. The top axis of Figs. 2(b) and 2(e) estimates the current density j necessary to induce such a generation rate in an emission active region of thickness D_{ar} assuming uniform carrier distributions,

$$\frac{j}{D_{ar}} = e \times G,\tag{1}$$

where e is the elementary charge. Active region thicknesses of 100 nm and 500 nm, therefore, correspond to current densities of 160 A/cm² and 800 A/cm² at 10^{26} cm⁻³ s⁻¹, respectively, under this approximation.

The increased efficiency of samples C and D relative to sample A implies that equivalent optical output can be achieved with less input. Figures 2(c) and 2(f) present the internal quantum efficiency as a function of the volumetric photon output rate, a quantity proportional to the optical output power. At 77 K, samples A, C, and D have peak internal quantum efficiencies that occur within 40% of one another in terms of photon output rate, compared to a factor of 3 in terms of carrier generation rate. At room temperature, these values change to 30% and a factor of 4, respectively. This implies that LEDs based on optimized InAs/GaSb, InAs/AlGaInSb, and the W-SL will have peak internal quantum efficiencies at similar radiances/output powers rather than similar currents. The internal quantum efficiency of sample D falls to the peak value for sample C at approximately a 30× higher photon generation rate at 77 K, suggesting that LEDs based on sample D would exhibit greatly enhanced wallplug efficiency for high-radiance applications because sample D maintains high internal quantum efficiency at much higher outputs rather than peaking at lower photon output, as is common in LEDs. 1,20

The exact underlying cause of the improvements observed in samples C and D requires knowledge of the carrier lifetimes in order to facilitate comparison of the internal quantum efficiency as a

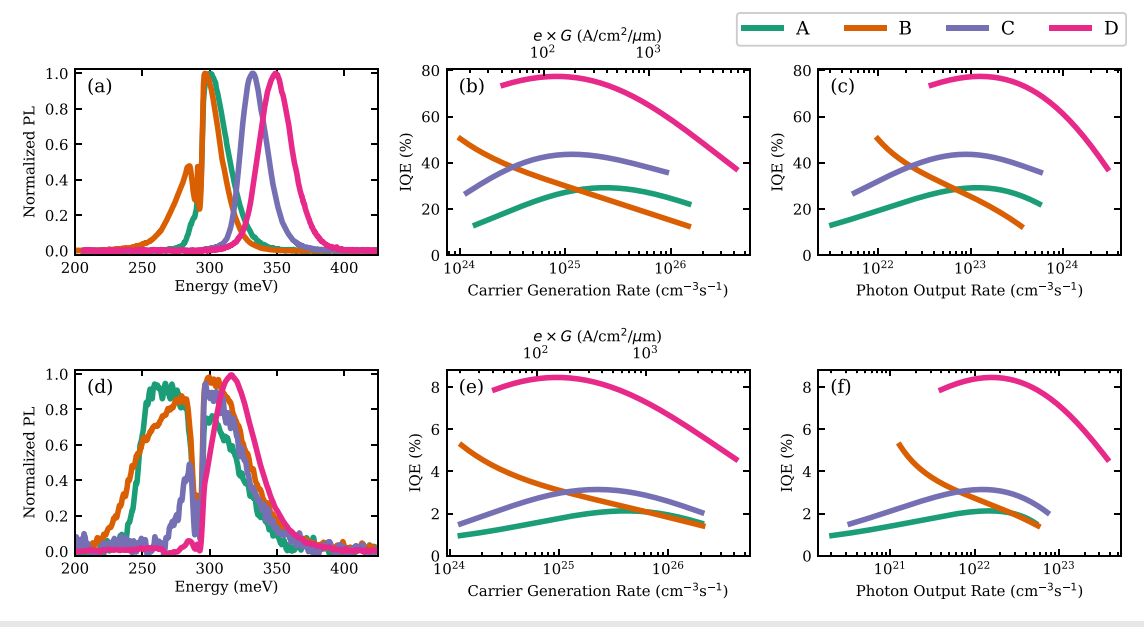


FIG. 2. Characterization results for each superlattice at (a)–(c) 77 K and (d)–(f) 293 K, including (a) and (d) spectrally resolved photoluminescence, (b) and (e) internal quantum efficiency as a function of carrier generation rate (bottom axis) and proportional to current (top axis), and (c) and (f) internal quantum efficiency as a function of the photon output rate.

function of excess carrier density. However, the causes can be inferred by applying the ABC model qualitatively. Within the ABC model and neglecting contributions from the background carrier density, the volumetric carrier generation rate can be written as

$$G(\Delta n) = A\Delta n + B\Delta n^2 + C\Delta n^3, \tag{2}$$

where Δn is the excess carrier density. At peak internal quantum efficiency, $\Delta n = \sqrt{A/C}$, and therefore, the carrier generation rate at peak internal quantum efficiency G^* is

$$G^* = A\left(2\sqrt{\frac{A}{C}} + \frac{B}{C}\right). \tag{3}$$

Similarly, the photon output rate $\mathcal P$ can be expressed as

$$\mathcal{P}(\Delta n) = \eta B \Delta n^2,\tag{4}$$

for η , the extraction efficiency. Therefore, the photon output rate at peak internal quantum efficiency \mathcal{P}^* is

$$\mathcal{P}^* = \eta \frac{AB}{C}.\tag{5}$$

These equations show that, for example, reductions in the Shockley–Read–Hall rate (A decreases) lower G^* and \mathcal{P}^* , while reductions in the Auger rate (C decreases) increase G^* and \mathcal{P}^* and an improvement to the radiative rate (B increases) increases G^* and \mathcal{P}^* . All these changes would also increase the internal quantum efficiency.

The qualitative application of the ABC model to the data in Fig. 2 suggests good agreement with the expectations from calculated band structures. Sample B illustrates an extreme case of a low Shockley–Read–Hall recombination rate and a high Auger recombination rate as G^* and \mathcal{P}^* occur at a lower values than our experimental

setup could measure; poor Auger recombination is expected for this sample due to the number of states in close proximity to the valence band Auger resonance. For samples C and D, the peak internal quantum efficiency increases relative to sample A, suggesting improved radiative or decreased non-radiative recombination; both samples C and D are expected to exhibit higher radiative recombination than sample A, and Auger recombination in sample D is expected to be highly suppressed. However, G^* decreases for samples C and D relative to A, while \mathcal{P}^* is approximately constant. Altogether, these features suggest that the increase in internal quantum efficiency is largely driven by the decrease in the Shockley–Read–Hall rate and the increase in the radiative rate; such changes favor lower G^* due to the $A^{3/2}$ and linear B dependence shown in Eq. (3), but make offsetting contributions to \mathcal{P}^* in Eq. (5). Carrier lifetime measurements are needed to unambiguously identify the root causes of the increased internal quantum efficiency.

In conclusion, we have investigated two mid-wave infrared superlattice designs, a four-layer superlattice and InAs/AlGaInSb, with greatly improved quantum efficiency at high injection compared to state-of-the-art superlattices, InAs/GaSb and InAs/InAsSb. Measurements of the internal quantum efficiency are in good agreement with the expectations based on the band structure. Superlattices have also been compared in terms of the carrier generation rate and photon output rate. The latter provides insight into the applicability of each superlattice for emitter applications, and the former underscores the potential of four-layer superlattices based on InAs/GaInSb/InAs/AlAsSb designs for high-radiance, high-efficiency mid-wave infrared LEDs

Any opinions, findings, and conclusions or recommendations expressed in this material are those of the author(s) and do not necessarily reflect the views of the Test Resource Management

Center (TRMC) Test and Evaluation/Science & Technology (T&E/S&T) Program and/or the U.S. Army Program Executive Office for Simulation, Training and Instrumentation (PEO STRI).

DATA AVAILABILITY

The data that support the findings of this study are available from the corresponding author upon reasonable request and with approval from PEO STRI.

REFERENCES

- ¹Y. Zhou, Q. Lu, X. Chai, Z. Xu, J. Chen, A. Krier, and L. He, Appl. Phys. Lett. 114, 253507 (2019).
- ²W. N. Carr, Infrared Phys. **6**, 1 (1966).
- ³K. J. Cheetham, A. Krier, I. P. Marko, A. Aldukhayel, and S. J. Sweeney, Appl. Phys. Lett. 99, 141110 (2011).
- ⁴P. J. Carrington, V. A. Solov'ev, Q. Zhuang, A. Krier, and S. V. Ivanov, Appl. Phys. Lett. 93, 091101 (2008).
- ⁵A. J. Muhowski, A. M. Muellerleile, J. T. Olesberg, and J. P. Prineas, J. Appl. Phys. **126**, 243101 (2019).
- ⁶O. M. Williams, Infrared Phys. Technol. 39, 473 (1998).
- ⁷A. Rogalski, M. Kopytko, and P. Martyniuk, Proc. SPIE **10177**, 1017715 (2017).
- ⁸D. L. Smith and C. Mailhiot, J. Appl. Phys. **62**, 2545 (1987).
- ⁹D. Donetsky, S. P. Svensson, L. E. Vorobjev, and G. Belenky, Appl. Phys. Lett. 95, 212104 (2009).
- 10 Y. Aytac, B. V. Olson, J. K. Kim, E. A. Shaner, S. D. Hawkins, J. F. Klem, M. E. Flatté, and T. F. Boggess, Appl. Phys. Lett. 105, 022107 (2014).
- ¹¹G. Ariyawansa, C. J. Reyner, E. H. Steenbergen, J. M. Duran, J. D. Reding, J. E. Scheihing, H. R. Bourassa, B. L. Liang, and D. L. Huffaker, Appl. Phys. Lett. 108, 022106 (2016).

- ¹²G. Ariyawansa, J. M. Duran, C. J. Reyner, E. H. Steenbergen, N. Yoon, D. Wasserman, and J. E. Scheihing, Proc. SPIE 10177, 1017712 (2017).
- ¹³J. R. Meyer, I. Vurgaftman, R. Q. Yang, and L. R. Ram-Mohan, Electron. Lett. 32, 45 (1996).
- ¹⁴I. Vurgaftman, R. Weih, M. Kamp, J. R. Meyer, C. L. Canedy, C. S. Kim, M. Kim, W. W. Bewley, C. D. Merritt, J. Abell, and S. Höfling, J. Phys. D: Appl. Phys. 48, 123001 (2015).
- ¹⁵L. Shterengas, T. Hosoda, M. Wang, T. Feng, G. Kipshidze, and G. Belenky, Electron. Lett. 17, 976703 (2016).
- ¹⁶S. Suchalkin, S. Jung, G. Kipshidze, L. Shterengas, T. Hosoda, D. Westerfeld, D. Snyder, and G. Belenky, Appl. Phys. Lett. 93, 081107 (2008).
- ¹⁷M. Ermolaev, Y. Lin, L. Shterengas, T. Hosoda, G. Kipshidze, S. Suchalkin, and G. Belenky, IEEE Photonics Technol. Lett. 30, 869 (2018).
- ¹⁸J. Abell, C. S. Kim, W. W. Bewley, C. D. Merritt, C. L. Canedy, I. Vurgaftman, J. R. Meyer, and M. Kim, Appl. Phys. Lett. **104**, 261103 (2014).
- ¹⁹C. S. Kim, W. W. Bewley, C. D. Merritt, C. L. Canedy, M. Warren, J. R. Meyer, and M. Kim, Opt. Eng. 57, 1 (2017).
- 20A. J. Muhowski, R. J. Ricker, T. F. Boggess, and J. P. Prineas, Appl. Phys. Lett. 111, 243509 (2017).
- ²¹R. J. Ricker, S. R. Provence, D. T. Norton, T. F. Boggess, and J. P. Prineas, J. Appl. Phys. **121**, 185701 (2017).
- Y. Aytac, B. V. Olson, J. K. Kim, E. A. Shaner, S. D. Hawkins, J. F. Klem, J. Olesberg, M. E. Flatté, and T. F. Boggess, J. Appl. Phys. 119, 215705 (2016).
- ²³E. H. Aifer, J. G. Tischler, J. H. Warner, I. Vurgaftman, W. W. Bewley, J. R. Meyer, J. C. Kim, L. J. Whitman, C. L. Canedy, and E. M. Jackson, Appl. Phys. Lett. 89, 053519 (2006).
- ²⁴S. A. Anson, J. T. Olesberg, M. E. Flatté, T. C. Hasenberg, and T. F. Boggess, J. Appl. Phys. 86, 713 (1999).
- ²⁵A. Chandola, R. Pino, and P. S. Dutta, Semicond. Sci. Technol. **20**, 886 (2005).
- ²⁶B. V. Olson, L. M. Murray, J. P. Prineas, M. E. Flatté, J. T. Olesberg, and T. F. Boggess, Appl. Phys. Lett. **102**, 202101 (2013).